Determining Material Parameters for Critical State Plasticity Models Based on Multilevel Extended Digital Database

Yang Liu
Department of Civil Engineering
and Engineering Mechanics,
Columbia University,
New York, NY 10027

WaiChing Sun[1]
Assistant Professor
Department of Civil Engineering
and Engineering Mechanics,
Columbia University,
New York, NY 10027
e-mail: wsun@columbia.edu

Jacob Fish
Department of Civil Engineering
and Engineering Mechanics,
Columbia University,
New York, NY 10027

This work presents a new staggered multilevel material identification procedure for phenomenological critical state plasticity models. The emphasis is placed on cases in which available experimental data and constraints are insufficient for calibration. The key idea is to create a secondary virtual experimental database from high-fidelity models, such as discrete element simulations, then merge both the actual experimental data and secondary database as an extended digital database (EDD) to determine material parameters for the phenomenological macroscopic critical state plasticity model. The calibration procedure therefore consists of two steps. First, the material parameters of the discrete (distinct) element method (DEM) simulations are identified via the standard optimization procedure. Then, the calibrated DEM simulations are used to expand the experimental database with new simulated loading histories. This expansion of database provides additional constraints necessary for calibration of the phenomenological critical state plasticity models. The robustness of the proposed material identification framework is demonstrated in the context of the Dafalias–Manzari plasticity model.
[DOI: 10.1115/1.4031619]

1 Introduction

Due to the complexity of granular material behaviors, phenomenological constitutive models must strike a balance between simplicity and predictability. While more comprehensive phenomenological models may be more robust and accurate for a given situation, the calibration of material parameters for such models are typically more complicated. Due to the larger set of internal variables required to describe the path-dependent behavior more accurate, comprehensive constitutive models often require a sizable datasets composed of multiple stress paths, loading and drainage conditions in order to generate sufficient constraints for calibrations. Nevertheless, the demand to generate, measure, store, and track the sufficient data through physical experiments can be costly and time consuming, and therefore, make the comprehensive models less appealing or even deemed to be impractical. The goal of this research is to accelerate the use of comprehensive constitutive models by means of an extended material database.

Over the past four decades, numerous constitutive models have been developed to describe the characteristic behavior of granular materials. The framework of elastoplastic modeling is well suited to simulate the path-dependent responses of granular materials, i.e., plastic strain, shear-dilatancy effects, stress-path dependency, pressure sensitivity, rotation of principal stress axes, fabric anisotropy, liquefaction and cyclic mobility, localization and shear banding [1–13]. The critical state concept in combination with the elastoplasticity theory has been rather successful for constructing simple and pertinent constitutive models for sand and other cohesionless granular materials [14–17]. Recently, these critical state models have been modified to incorporate stress anisotropy due to the evolution of fabric, and the anisotropic kinematic hardening responses for cyclic loading [18–22]. The improved accuracy, nevertheless, comes with the price of increased material parameter set. Consequently, it becomes no longer feasible to identify material parameters by visual inspection. Instead, one must constitute a constrained optimization problem designed to identify material parameters that minimizes the errors of numerical simulations characterized by an objective function and a set of constraints through an iterative process [23]. The discrepancy between experimental data and numerical simulations in a least square sense comprises the objective function, which depends on constitutive law parameters. An optimization algorithm, such as the gradient-based methods [24,25], swarm intelligence-based algorithms [26,27], and neural networks [28], is employed to seek material parameters that minimize the error defined by the objective function. There have been a number of attempts to calibrate constitutive model parameters for sands (e.g., Toyoura sand [29,30], Nevada sand [25,31,32], and pea-gravels [33]). Various material identification schemes [34,35] adopted finite element based inverse analysis to account for spatial heterogeneity. By utilizing a spatially dependent objective function, these algorithms exploit information from measured inhomogeneous deformation fields in comparison to the finite element solution to identify material parameters. This approach [36] has been recently employed to identify material parameters for granular materials by utilizing full-field displacement measurements. Spatially varying constitutive model parameters can be obtained from such a calibration process.

---

[1]Corresponding author.

The identification of material parameters for phenomenological constitutive laws relies heavily on experimental data obtained from laboratory tests or field studies. Since the cost and time involved to conduct physical tests required for calibration of material parameters is quite prohibitive, a widespread adoption of comprehensive models in practice is quite limited. For instance, to identify the shape and size of a yield surface, one may need to record the yield stress for multiple stress paths with different confining pressures. Such an extensive experimental data is rarely justifiable in practice due to considerable cost involved. A more cost-efficient alternative is to conduct only a limited numbers of tests and replace the rest of tests with virtual high-fidelity simulations. For instance, a small-scale physics-based high-fidelity model can be used to generate the required computational (virtual) data, which is then merged with an available limited experimental data to form so-called an EDD. Experiments (both laboratory and virtual) housed in the EDD are then used to explore the new features of the comprehensive phenomenological constitutive material models and to identify their parameters. Such a framework is one of the key components of the integrated computational material engineering [37], with a wide variety of engineering applications ranging from informatics-based material design to comprehensive data mining tools [38,39] and wing design optimization in aerodynamics [40,41].

In this study, we propose a staggered multilevel approach to identify material parameters for macroscopic phenomenological model with limited or insufficient available experimental data. The key idea is to use high-resolution or other detailed simulations to supplement the missing experimental data essential for material identifications. To supplement the experimental data, a high-fidelity model is first calibrated with the available experimental data, then employed to run additional simulations to create a secondary virtual experimental data, which supplements the true experimental data. With the extended database consisting of both true and virtual experimental data, the optimal material parameter set can be identified via a constrained optimization algorithm.

In this work, our focus is on applying the EDD concept to granular materials. As a result, we use the grain-scale DEM as the tool to obtain high-fidelity simulated data and extend the digital database, while a macroscopic critical state plasticity model proposed by Dafalias and Manzari [30] (referred as DaMa model herein) is calibrated via the EDD and served as the low-fidelity model calibrated for forward predictions made with limited computational costs. The details of the calibration procedure are described in the following steps:

(i) The high-fidelity model (DEM) is first calibrated with the available laboratory experimental database to find material parameters of the DEM model that minimizes the discrepancy between the experimental data and responses simulated by the high-fidelity model.

(ii) The EDD is formed by supplementing the experimental data with the simulated responses obtained from the DEM models to provide essential additional constraints for the low-fidelity DaMa model.

(iii) The material parameters of the low-fidelity DaMa model are identified using an optimization algorithm that minimizes the discrepancy between the responses from the EDD database and those simulated by the DaMa model.

(iv) Once calibrated, the DaMa model is ready for forward predictions.

The DEM simulations of monotonic and cyclic torsion, directional shear, and various triaxial loads are used to expand the experimental database. The critical state two-surface plasticity model pioneered by Dafalias and Manzari [30], which incorporates the fabric-dilatancy effect, is used for proof of concept as a low-fidelity model in comparison to the DEM. The present manuscript focuses on the Nevada sand for which experimental data is available.

The rest of the paper is organized as follows. The proposed material identification framework and the salient features of the EDD-based material identification procedure are introduced in Sec. 2, followed by the formulations of the variable-fidelity models, including the DEM and Dafalias–Manzari critical state plasticity model. By using Nevada sand as the test bed, the step-by-step implementation of the proposed multilevel material identification procedure is demonstrated in Secs. 3 and 4. In particular, Sec. 3 presents the calibration of the DEM assemblies and the formation of the EDD. Numerical experiments that calibrate the DaMa model to the EDD are then presented in Sec. 4. To investigate the robustness and effectiveness of the proposed approach, an assessment of forward prediction of calibrated DaMa model is conducted in Sec. 5. Finally, conclusions are drawn in Sec. 6.

2 The Variable Fidelity Model Framework

2.1 Description of the Proposed Algorithm. The proposed multilevel calibration approach synthesizes both microscale and macroscale analyses, as is shown in Fig. 1. In the microscale analysis, a calibration of the geometric and micromechanical parameters of the DEM assemblies based on the experimental data is carried out. The calibrated DEM assemblies are subsequently used to expand the experimental database with new simulated loading histories, creating an extended database that
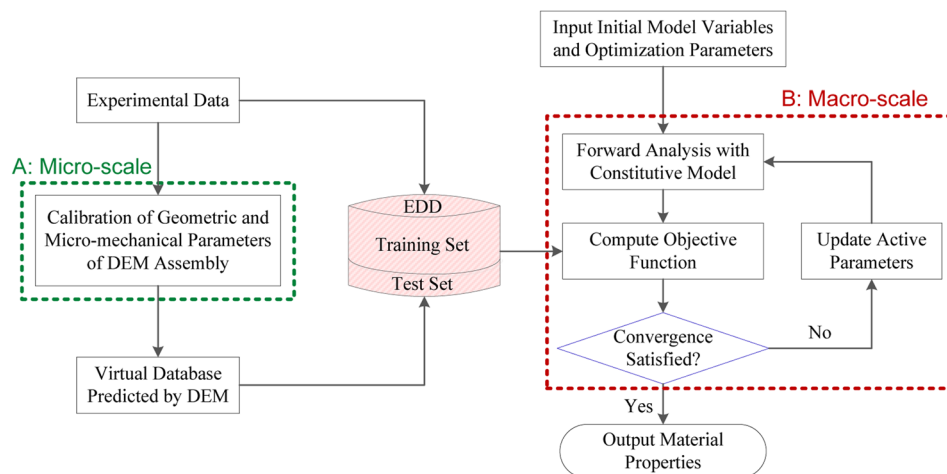

Fig. 1 The flowchart of the proposed multilevel material identification procedure using EDD and optimization

combines the virtual and physical experimental data. This combined dataset is then used to calibrate phenomenological constitutive model by solving the inverse problem with digital and experimental database that comprise the EDD as constraints.

To test whether the calibrated phenomenological model is predictive, experimental data in the EDD is split into two sets: (1) the training set, which is used for inverse calibration of the phenomenological constitutive model, and (2) the verification (test) set, which compares experimental data not included in the first set with the simulated response to assess the accuracy and robustness of forward predictions. The EDD provides the necessary dataset for calibration of multiparameter phenomenological model, such as DaMa.

2.2 High-Fidelity Micromechanics Model: DEM. In the proposed calibration framework, we use DEM as the high-fidelity model to expand the experimental data. First proposed by Cundall and Strack [42], the DEM has been widely used to investigate micromechanical features of the granular assemblies. In a DEM assembly, the translational and rotational motions of each particle are obtained by the force and momentum equilibrium equations

$$m^J \ddot{\mathbf{u}}^J = \sum (\mathbf{f}^{IJ} + \mathbf{D}^{IJ}) - C_g \dot{\mathbf{u}}^J$$
$$I^J \ddot{\boldsymbol{\theta}}^J = \sum \mathbf{M}^{IJ} - C_g^* \dot{\boldsymbol{\theta}}^J \quad (1)$$

where m^J and I^J are mass and moment of inertia of particle J, respectively; $\ddot{\mathbf{u}}^J$ and $\ddot{\boldsymbol{\theta}}^J$ are translational and rotational accelerations, $\mathbf{f}^{IJ}$ and $\mathbf{M}^{IJ}$ are interparticle force and moment, respectively, exerted on particle J from particle I at contact, $\mathbf{D}^{IJ}$ is contact damping force comprising of normal, $\mathbf{D}_n^{IJ}$, and tangential, $\mathbf{D}_s^{IJ}$, components at the contacts, defined as

$$\mathbf{D}_n^{IJ} = c_n \dot{\mathbf{n}}; \quad \mathbf{D}_t^{IJ} = c_s \dot{\mathbf{s}} \quad (2)$$

where $\dot{\mathbf{n}}$ and $\dot{\mathbf{s}}$ are normal and tangential components of the relative velocities between particles I and J; here, c_n and c_s are the corresponding contact damping coefficients. C_g and C_g^* are the coefficients of global damping operating on particle velocities $\dot{\mathbf{u}}^J$ and $\dot{\boldsymbol{\theta}}^J$, respectively [42]. The contact and global damping in the DEM simulations are chosen to adequately damp the higher frequency modes without excessively delay particle motions [43].

The DEM simulation explicitly models the kinetics of individual grains via interparticle contact laws. In our implementation, we adopt the Jäger contact model [44–46] with a general contact profile in which the sphere is assumed to have a specific local irregularity of the form $A_\alpha r^\alpha$ at the contact region, as shown in Fig. 2(a).

In the Jäger contact model, the normal force between an asperity of a general form and a hard flat surface is defined as

$$f^n = C_\alpha \zeta^{(1+\alpha^{-1})}, \quad C_\alpha = \frac{4\alpha G_s}{(1-\nu_s)(1+\alpha)} \left(\frac{\Gamma((1+\alpha)/2)}{\sqrt{\pi} A_\alpha \Gamma(1+\alpha/2)} \right)^{\alpha^{-1}} \quad (3)$$

where ζ denotes the indentation at contact (half of the contact overlap); G_s and ν_s are shear modulus and Poisson's ratio of the grains, respectively; and Γ is the gamma function; α is a variable that describes the local irregularity of contact. Equation (3) yields the standard Hertz solution if $\alpha = 2$ and $A_2 = 1/(2R)$, representing Hertzian contact along ideally smooth spherical surfaces (Fig. 2(a)). With a conical asperity with $\alpha = 1$, A_1 corresponds to the outer slope of the cone (Fig. 2(b)).

The tangential force between two contacting particles is computed with an extension of the Hertz–Mindlin–Deresiewicz theory, which accounts for three-dimensional arbitrary normal and tangential contact movements. The detailed theoretical argument and numerical implementation are presented in Refs. [45] and [46]. The equations of motion in Eq. (1) are solved via an explicit central difference algorithm. Within each incremental updates for the displacement and rotation of each particle, scaled time parameter and unit mass are used to obtain quasi-static responses via dynamics relaxation [47].

For a unit cell composed of a collection of particles, the macroscopic Cauchy stress tensor of the particle assemblies can be recovered vis spatial homogenization [48], virtual work principle [49], or generalized mathematical homogenization [47], which all lead to

$$\sigma_{ij} = \frac{1}{V} \sum_{n=1}^{N_c} l_i^n f_j^n \quad (4)$$

where f_j^n is the contact force at contact point n; l_i^n is the branch vector connecting the centers of two contacting particles at n, and N_c the total number of contacting particle pairs in the volume V of the unit cell.

To expand the material database using DEM, one must first calibrate the material parameter of the particle and generate granular assemblies using the physical experimental data. Following this calibration step, the DEM is employed to expand the material database for a specific type of granular materials, such as sand and slit.

2.3 Low-Fidelity Phenomenological Model: Dafalias–Manzari Critical State Plasticity. In this study, we adopt the model proposed by Dafalias and Manzari in Ref. [30] as the low-fidelity phenomenological model and calibrate it with the expanded database. Notice that the multilevel calibration framework proposed in this study is also applicable to other critical state plasticity models for granular materials (e.g., Refs. [50–53]). The Dafalias–Manzari model is selected, as the test bed, because it is relatively easy to
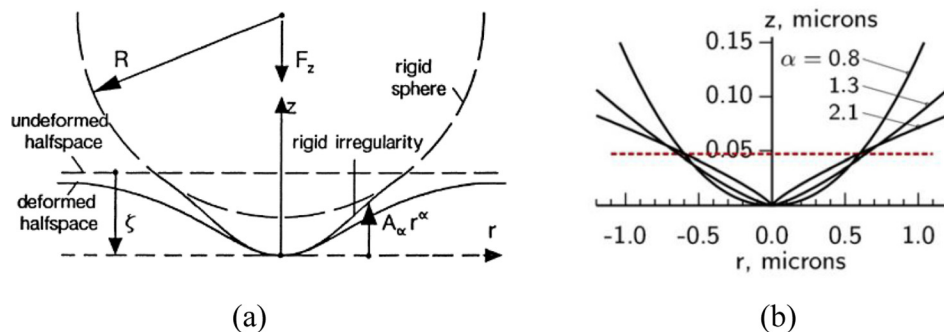

Fig. 2 Contours of contact asperities (a) general power-form surface contour $z = A_\alpha r^\alpha$ [44]; (b) surface contour with different asperities used in DEM simulations (Reproduced with permission from Kuhn et al. [71]. Copyright 2014 by Matthew R. Kuhn, Professor, Dept. of Civil Engineering, Donald P. Shiley School of Engineering, Univ. of Portland, Portland, OR).

implement and has been widely adopted. To enhance the accuracy and predictability of the phenomenological model, a larger set of material parameters is typically required to govern the evolutions of internal variables. For comprehensive phenomenological models for granular materials, such as the critical state plasticity model of Dafalias and Manzari [30] considered in this study, considerable experimental database is required to identify the loci of yield surface and the size and shape of the limited surfaces.

Dafalias and Manzari [30] model (DaMa) is a comprehensive critical state plasticity model employing state parameters for modeling mechanical behavior at various densities and confining pressures under monotonic and cyclic loading conditions. It combines the concepts of bounding surface model and critical state generalized plasticity concept to form an elegant model that accounts for fabric-dilatancy quantity and the effect of fabric changes to predict stress–strain relations under various drainage and loading conditions. For completeness, the multi-axial formulation of the DaMa model is briefly described in this section. Interested readers are referred to the original papers cited above.

In the DaMa model [30], the strain increments are additively decomposed into elastic and plastic parts. The elastic parameters G_0 and ν define the nonlinear hypo-elastic behavior by

$$G = G_0 p_{at} \frac{(2.97 - e)^2}{1 + e} \left(\frac{p}{p_{at}}\right)^{1/2}; \quad K = \frac{2(1 + \nu)}{3(1 - 2\nu)} G \quad (5)$$

where G_0 is a material constant, ν is the Poisson's ratio, e is the current void ratio, and p_{at} is the atmospheric pressure. Both G_0 and ν are independent of applied stress path and can be obtained from small strain monotonic shearing behavior.

The yield surface is defined as

$$f(\sigma, \alpha, m) = (r_{ij} r_{ij})^{1/2} - \sqrt{2/3} mp = 0 \quad (6)$$

$$r_{ij} = (s_{ij} - \alpha_{ij}) \quad (7)$$

where m is the size of the yield surface, s_{ij} is the deviatoric stress tensor, and α_{ij} is the deviatoric back stress tensor which describes the kinematic hardening of the yield surface by indicating the location of the center of the yield surface.

The critical state of a soil [15] refers to a continuous flow state with constant stress and constant volume in granular soil. In this model, the critical state of a soil [54] is defined to satisfy simultaneously the conditions $q = q_c$, $p = p_c$, $e = e_c$, $q_c/p_c = M$ as well as the equation of critical state line (CSL) in $e - p$ space [55]

$$e_c = e_0^c - \lambda_c \left(\frac{p_c}{p_{at}}\right)^\xi \quad (8)$$

where q_c, p_c, M, e_0^c, λ_c, and ξ are scalar parameters obtained from interpolating the mean stress $p = (\sigma_1 + 2\sigma_3)/3$, deviatoric stress $q = \sigma_1 - \sigma_3$ and the void ratio e at the critical state. Here, e_0^c denotes the void ratio at $p_c = 0$. The bounding surface is associated with the maximum peak stresses ratio state that can be attained, and the dilation surface represents the condition at which the contractive soil behavior changes to dilative. The bounding surface and the dilation surface are constructed to comply with the critical state theory in the following form which are dependent on the Lode angle θ:

$$\alpha_{\theta ij}^a = \sqrt{2/3} \alpha_\theta^a n_{ij}; \quad n_{ij} = r_{ij} / \sqrt{(r_{ij} r_{ij})} \quad (a = b, c, d) \quad (9)$$

$$\alpha_\theta^b = g(\theta, c) M \exp(-n^b \psi) - m \quad (10)$$

$$\alpha_\theta^d = g(\theta, c) M \exp(n^d \psi) - m \quad (11)$$

$$\alpha_\theta^c = g(\theta, c) M - m \quad (12)$$

$$g(\theta, c) = \frac{2c}{(1 + c) - (1 - c)\cos 3\theta}; \quad c = \frac{M_e}{M_c} \quad (13)$$

where the superscript a may take three values of b (for bounding surface), d (for dilatancy surface), and c (for critical surface); n^b and n^d are positive scalar constants which control the size of the two limit surfaces, respectively; $g(\theta, c)$ is the scaling function used for generalization of surfaces from triaxial space to multiaxial space; and c is referring to the ratio between the critical state stress ratios in compression and extension. For simplicity, c is a common parameter for all three surfaces. It is seen from Eqs. (9)–(11) that the bounding and dilation surfaces tend to coincide with the critical state surface as $\psi \to 0$. The yield surface governed by pure kinematic hardening law translates in the stress space. The state parameter $\psi = e - e_c$ proposed by Been and Jefferies [56] is used to measure the distance from the current state to the critical state.

The evolution of hardening modulus K_p and plastic dilatancy D is described as functions of the relative distance between the image back stress ratios, $\alpha_{\theta ij}^b$ and $\alpha_{\theta ij}^d$, respectively, and the back stress of the yield surface α_{ij}, given by

$$K_p = \frac{2}{3} ph \left(\alpha_{\theta ij}^b - \alpha_{ij}\right) n_{ji} \quad (14)$$

$$D = A_d (\alpha_{\theta ij}^d - \alpha_{ij}) n_{ji} \quad (15)$$

where h is a positive scaling function defined by positive constants h_0 and c_h

$$h = b_0 / [(\alpha_{\theta ij}^b - \alpha_{ij}^{in}) n_{ji}] \quad \text{with} \quad b_0 = G_0 h_0 (1 - c_h e)(p/p_{at})^{-1/2} \quad (16)$$

And the positive scaling function A_d for dilatancy is affected by the fabric changes such that

$$A_d = A_0 (1 + \langle z_{ij} n_{ji} \rangle) \quad \text{with} \quad \dot{z}_{ij} = -c_z \langle -\dot{\varepsilon}_v^p \rangle (z_{max} n_{ij} + z_{ij}) \quad (17)$$

where z_{ij} denotes the fabric-dilatancy internal variable, A_0 and z_{max} are material constants which control the pace of evolution of z_{ij}. The Macauley brackets $\langle \ \rangle$ representing $\langle x \rangle = x$ if $x > 0$ and $\langle x \rangle = 0$ if $x \le 0$. Equations (14)–(17) dictate the mechanism of the effect of fabric change on dilatancy upon load increment reversals.

Therefore, a total set of 15 model parameters are required to completely define the DaMa model. These parameters can be categorized into three groups, namely, elastic parameters, critical state parameters, and model specific parameters [33,57,58]. The parameters in each group are:

- elastic parameters: G_0 and ν
- critical state parameters: M, c, λ_c, e_0^c, and ξ
- model specific parameters: yield surface parameter m, hardening constants $\{h_0, c_h, n^b\}$, dilatancy constants $\{A_0, n^d\}$, and fabric-dilatancy constants $\{z_{max}, c_z\}$

2.4 Calibration Through Constrained Optimization. The parameter identification process is formulated as a constrained optimization problem in which the objective is to identify an optimal set of parameters that minimizes the discrepancy between the simulated response by DaMa and the data housed in EDD in the least square sense. In other words, the optimization problem is an iterative process in which material parameters are modified in each trial based on the results of the inverse problem until the predicted data best fits the target data housed in EDD.

Let us denote the model parameters to be calibrated by $\theta \in \mathbb{R}^{N \times 1}$, where N is the total number of parameters. In the present study, θ consists of 15 DaMa model parameters ($N = 15$), i.e., $\theta = \{G_0, \nu, M, c, \lambda_c, e_0^c, \xi, m, h_0, c_h, n^b, A_0, n^d, z_{max}, c_z\}^T$.

We define an objective function representing the discrepancy between the target response quantities from EDD and the predicted data obtained by DaMa model as

$$f(\boldsymbol{\theta}) = \frac{1}{2}\mathbf{r}^{\mathrm{T}}(\boldsymbol{\theta})\mathbf{W}\mathbf{r}(\boldsymbol{\theta}) \qquad (18)$$

where $\mathbf{r}(\boldsymbol{\theta}) \in \mathbb{R}^{SL \times 1}$ is the residual vector and $\mathbf{W} \in \mathbb{R}^{SL \times SL}$ is the diagonal weight matrix, given by

$$\mathbf{r}(\boldsymbol{\theta}) = \begin{Bmatrix} \hat{\mathbf{y}}_1(\boldsymbol{\theta}) - \mathbf{y}_1 \\ \hat{\mathbf{y}}_2(\boldsymbol{\theta}) - \mathbf{y}_2 \\ \vdots \\ \hat{\mathbf{y}}_S(\boldsymbol{\theta}) - \mathbf{y}_S \end{Bmatrix}; \quad \mathbf{W} = \begin{bmatrix} \frac{w_1}{\mathbf{y}_1^T\mathbf{y}_1}\mathbf{I} & & & 0 \\ & \frac{w_2}{\mathbf{y}_2^T\mathbf{y}_2}\mathbf{I} & & \\ & & \ddots & \\ 0 & & & \frac{w_S}{\mathbf{y}_S^T\mathbf{y}_S}\mathbf{I} \end{bmatrix} \qquad (19)$$

in which $\mathbf{y}_i = \{y_{i1}, y_{i2}, ..., y_{iL}\}^{\mathrm{T}}$ and $\hat{\mathbf{y}}_i(\boldsymbol{\theta}) = \{\hat{y}_{i1}(\boldsymbol{\theta}), \hat{y}_{i2}(\boldsymbol{\theta}), ..., \hat{y}_{iL}(\boldsymbol{\theta})\}^{\mathrm{T}}$ are the target response quantities and the predicted data, respectively, of the ith data set ($i = 1, 2, ..., S$); w_i is the weight coefficient of the ith data set; $\mathbf{I} \in \mathbb{R}^{L \times L}$ is an identity matrix; S is total number of target data sets; and L is total number of data points of the target response quantities.

For example, in our implementation, both the stress–strain behavior and the evolution of void ratio are considered in the curve fitting process for each test (e.g., $L = 2$). Thus, the target response quantities and the predicted data can be expressed as

$$\mathbf{y}_i = \left\{\frac{q_i}{p_0}, e_i\right\}^{\mathrm{T}} \quad \text{and} \quad \hat{\mathbf{y}}_i(\boldsymbol{\theta}) = \left\{\frac{\hat{q}_i(\boldsymbol{\theta})}{p_0}, \hat{e}_i(\boldsymbol{\theta})\right\}^{\mathrm{T}} \qquad (20)$$

where q denotes the deviatoric stress, p_0 is the initial mean stress, and e is the void ratio.

The goal is to minimize the objective function $f(\boldsymbol{\theta})$ and to obtain the best set of model parameters. Therefore, the constrained optimization problem can be stated as

$$\hat{\boldsymbol{\theta}} = \arg \min_{\boldsymbol{\theta}}\{f(\boldsymbol{\theta})\} \quad \theta_j^{\mathrm{lb}} \le \theta_j \le \theta_j^{\mathrm{ub}} \ (j = 1, 2, ..., N) \qquad (21)$$

where θ_j^{lb} and θ_j^{ub} denote the lower and the upper bound of the jth parameter, and $\hat{\boldsymbol{\theta}}$ denotes the calibrated model parameters that best fit the target database.

We employ the Gauss–Newton trust region algorithm [59] to solve the optimization problem in Eq. (21). In the optimization process, the parameters are updated by the iterative process given by

$$\hat{\boldsymbol{\theta}}_{k+1} = \hat{\boldsymbol{\theta}}_k - (\hat{\mathbf{J}}_k^{\mathrm{T}}\hat{\mathbf{W}}\hat{\mathbf{J}}_k + \lambda\mathbf{I})^{-1}\hat{\mathbf{J}}_k^{\mathrm{T}}\hat{W}\,\hat{r}\,(\boldsymbol{\theta}_k) \qquad (22)$$

where k is the iteration number index; $\hat{\boldsymbol{\theta}}_k$ denotes the active parameter set (i.e., $\hat{\boldsymbol{\theta}}_k \in \boldsymbol{\theta}_k$); λ is the Levenberg–Marquardt parameter [60] which can be determined iteratively; $\hat{r}$ and $\hat{\mathbf{W}}$ contain components of $\mathbf{r}$ and $\mathbf{W}$, respectively, for model parameters inside the bounds; $\hat{\mathbf{J}}_k$ is the Jacobian of $\hat{r}(\boldsymbol{\theta}_k)$, namely, $\hat{J}_k^{pj} = \partial\hat{r}_p(\boldsymbol{\theta}_k)/\partial\theta_j$, where $p = 1, 2, ..., SL$ and $j = 1, 2, ..., N$. Herein, we approximate the Jacobian components using central difference method, viz.,

$$\hat{J}^{pj} \approx \frac{\hat{r}_p(\theta_1, ..., \theta_{j-1}, \theta_j + \delta\theta_j, \theta_{j+1}, ..., \theta_N) - \hat{r}_p(\theta_1, ..., \theta_{j-1}, \theta_j - \delta\theta_j, \theta_{j+1}, ..., \theta_N)}{2\delta\theta_j} \qquad (23)$$

where $\delta\theta_j$ is an infinitesimal perturbation. It is noteworthy that Eq. (23) is guided by an active parameter strategy, which imposes simple bounds on the trust region represented by radius Δ [59]. In addition, λ is selected to ensure that the solution updates lie within the trust region. The two parameters λ and Δ are computed using a locally constrained hood step algorithm [61].

The optimization is completed and a set of parameter $\hat{\boldsymbol{\theta}}$ is returned when the following criteria are satisfied:

$$C_1 = f(\boldsymbol{\theta}_k) \le 0.01 \text{ and } C_2 = \|\hat{\mathbf{J}}_k^{1:SL,j}\| \le 1 \times 10^{-8} \ (j = 1, 2, ..., N) \qquad (24)$$

where $\|\bullet\|$ denotes the L_2 norm of a vector and $1:SL$ denotes the first SL rows in a matrix.

3 Calibration and Prediction of DEM Model

In this study, we test the proposed multilevel calibration procedure with the Nevada sand dataset from published literature. We choose the Nevada sand as the test bed due to the large amount of existing data generated in the past decades. For this purpose, laboratory tests performed on this sand by Earth Technology Corporation in the course of the Verification of Liquefaction Analysis by Centrifuge Studies project [62] were used. The objective is to use well-calibrated DEM assemblies as virtual specimens and conduct high-fidelity microscale (DEM) simulations on those

DEM assemblies to generate the necessary constraints to calibrate the DaMa model when experimental data alone is insufficient. The generalized procedure of the calibration process can be described as follows: (i) construct DEM assemblies with the goal of approximating the behavior of Nevada sand, (ii) calibrate the DEM model parameters based on the lab experimental data, (iii) carry out DEM simulations subjected to loading paths that are not considered in the lab tests, (iv) expand the database by adding the DEM simulated responses to the experimental database and form the EDD, and (v) calibrate the constitutive model parameters based on the EDD.

In this section, the DEM assemblies are created and calibrated to approximate the behavior of Nevada sand at different relative densities and confining pressures against the experimental data from lab test reports [62,63]. The DEM simulations were conducted using the open source DEM code OVAL [64].

3.1 Representative Volume Element (RVE) Generation. The macroscopic mechanical behavior of granular materials depends on both the material properties of particles and the topological features of the grain assemblies. The DEM provides a convenient tool to explicitly model this particulate nature but is also more computationally expensive than continuum model. As a result, the DEM is chosen as the high-fidelity model to expand the material database. In this study, we assume that the material database contains only macroscopic constitutive responses obtained

Table 1 Physical properties of Nevada sand and DEM assemblies used in this study

Sample	Mean grain size D_{50} (mm)	Uniformity coefficient $C_u = D_{60}/D_{10}$	Maximum void ratio $e_{\min}$	Minimum void ratio $e_{\max}$	Void ratio at different D_r		
					$e_{D_r=40\%}$	$e_{D_r=60\%}$	$e_{D_r=89\%}$
Nevada sand [62]	0.165	2.2	0.511	0.887	0.736	0.661	0.552
DEM assembly	0.165	2.0	0.525	0.850	0.720	0.655	0.560

from conventional shear, plane strain and triaxial loading experiments. Microscopic data that require unconventional experimental techniques to obtain (e.g., position vectors of individual particles, topology of void space, and the scale of fluctuation of material parameters within specimen) are not considered [65–68]. Such a consideration is reasonable for engineering practice in which microscopic data are rarely extracted or used due to the associated cost.

Since we do not employ any microscopic data that explicitly captures the geometry of individual grains, we will not attempt to use the corresponding DEM models, such as the level-set based potential element method [69] and nonuniform rational basis spline-based granular element method [70], to generate granular assemblies that are compatible to the experimental counterpart on a grain-by-grain basis. Instead, our goal is to generate RVE that has the compatible initial relative density, grain size distribution, and constitutive responses to those of the experimental counterpart. In this study, we adopt the particle assemblies from Ref. [71], which are composed of bumpy particles formed by lumping overlapped spheres together. As shown in Ref. [72], those assemblies composed of bumpy particles may yield more realistic friction angles and macroscopic shear strength than those composed of spherical particles. Since the angularity and nonsymmetry of particle shape can be properly replicated, this leads to improvement in capturing the interlocking among particles and the greater resistance of particle rotation. As a result, the increase in the deviatoric stress to the peak value and in the volumetric strain with the angularity commonly observed in experiments can be replicated with bumpy particles.

In this study, a bumpy, compound cluster shape with a large central sphere with six embedded satellite spheres in an octahedral arrangement was chosen, which was studied and presented by Kuhn et al. [71]. This shape has proven to be sufficiently nonround to produce a target range of initial densities and realistic strength. A total number of 6400 bumpy elements from an assembly represents a unit cell at the material point, which are found to be large enough to capture the overall stress–strain response of material but sufficiently small to prevent mesoscale localization and boundary-condition-induced nonuniformities (e.g., shear bands, footings, excavations) [71].

The particles in the grain assembly are scaled such that the grain size distribution of the DEM assembly is close to those of the real Nevada sand. The resultant virtual specimen has a grain size distribution with median particle size $D_{50} = 0.165$ mm and a coefficient of uniformity $C_u = 2.0$, comparing with the laboratory tests data $D_{50} = 0.165$ mm and $C_u = 2.2$ [62] (see Table 1). A comparison of the physical properties between lab test samples for Nevada sand and the DEM assembly of virtual particles are shown in Table 1.

The 6400 bumpy particles were initially sparsely distributed in a space cell surrounded by period boundaries. By repeatedly assigning random velocities to particles and reducing the assembly height, 15 assemblies with initial void ratios in the range of 0.850–0.525 were created. Each assembly was then isotropically consolidated to a target mean effective stress from 10 kPa to 400 kPa for subsequent computations involving microparameter calibration and digital database enrichment. It is noted that tests under even higher consolidation stresses may lead to particle breakage and grain crushing [73–75] when the stress applied on the soil particle exceeds its strength, which is beyond the scope of this study.

Due to the disparity in shapes between natural sand and DEM particles, the real and numerical specimens may have different ranges of attainable porosity. As a result, minimizing the discrepancy of the numerical and experimental void ratios may not lead to comparable state condition in granular materials. Alternatively, we conduct a numerical relative density test to obtain the maximum and minimum void ratio of the granular assemblies, and the notion of relative density was chosen as a measure of equivalence to match experimental and numerical results [72]

$$D_r = \frac{e_{\max} - e}{e_{\max} - e_{\min}} \qquad (25)$$

where void ratio e can be obtained from relative density D_r through the maximum void ratio $e_{\max}$ and minimum void ratio $e_{\min}$ that a sand sample could achieve with standard ASTM procedures [76,77]. The corresponding void ratios at three different relative densities used in the following simulations are shown in Table 1. It is noteworthy that, to compare the results quantitatively, the simulations were accomplished on samples with identical or nearly identical relative densities compared with those in target experimental tests.

3.2 Calibration of the Micromechanical Properties of DEM Assemblies. The micromechanical properties of the aforementioned DEM assemblies have been calibrated by Kuhn et al. [71] to capture cyclic liquefaction behavior of Nevada sand. The calibration efforts attempt to produce a relationship between small-strain bulk shear modulus $G_{\max}$ and the mean effective stress p' (i.e., $G_{\max} = (p')^{0.5}$), and to achieve $G_{\max}$ with a target value of 90 MPa at a mean effective stress of 80 kPa [78,79]. The same set of model parameters obtained by Kuhn et al. [71] was used throughout all the DEM simulations in this study, as shown in Table 2. For detailed processes on particle assembly preparation and guidance on model parameter calibration, readers are referred to Refs. [71], [72], and [80].

A series of undrain and drained triaxial compression (TC) and extension simulations were carried out on the samples studied above. The shear stress–strain (octahedral) responses recorded during the computations were compared to experimental data [62] in Figs. 3–10.

To match the monotonic undrained TC and extension tests for Nevada sand at 40% D_r, two assemblies with initial void ratios (0.732 and 0.707) that straddle the target void ratio $e_0 = 0.720$ (see Table 1) were considered. Before triaxial loading, the assemblies were isotropically consolidated to the mean effective stress p'_0 corresponding to the experiments' confining stresses, e.g.,

Table 2 Micromechanical parameters for DEM computations

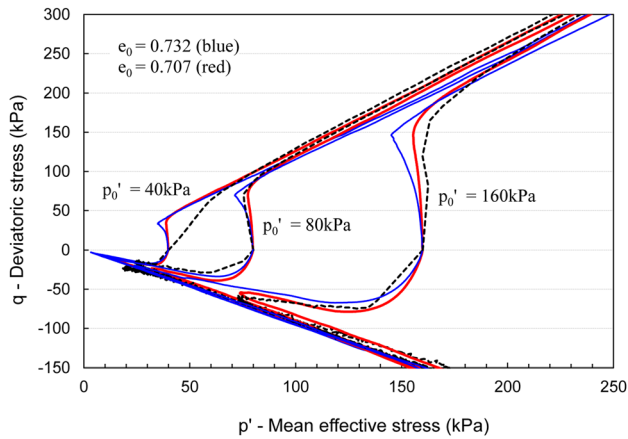|	
29.0	Shear modulus G (GPa)
0.15	Poisson ratio
0.60	Coefficient of friction at particle–particle and particle–wall contacts
0.20	Viscosity coefficient for translational body damping
0.30	Viscosity coefficient for rotational body damping
0.00	Viscosity coefficient for contact damping
5.3	Jäger contact model parameter A_1
1.3	Jäger contact model parameter α

Fig. 3 Undrained TC and extension of DEM simulations at three densities, comparing with Nevada sand tests (black dashed lines) at relative density of 40% with initial confining pressure of 40 kPa, 80 kPa, and 160 kPa (stress paths)
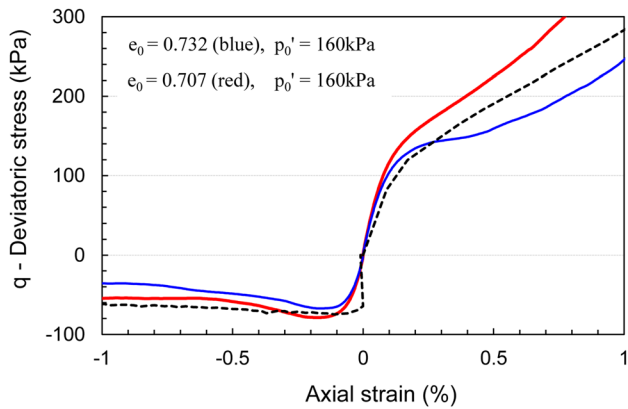

Fig. 4 Undrained TC and extension of DEM simulations at three densities, comparing with Nevada sand tests (black dashed lines) at relative density of 40% with initial confining pressure of 160 kPa (stress–strain curves)

Fig. 5 Drained TC (constant p') of DEM simulations at $e = 0.732$, comparing with Nevada sand tests at relative density of 40% with initial confining pressure of 40 kPa, 80 kPa, and 160 kPa: (a) stress paths and (b) volumetric curves

40 kPa, 80 kPa, and 160 kPa, respectively. The mean effective stress p' was computed from initial confining pressure and pore-water pressure (PWP) $p' = p - u$. Loading was applied in the z direction with a small strain increment $\Delta\varepsilon_{zz} = \pm 5.0 \times 10^{-7}$ to maintain nearly quasi-static conditions. For undrained tests, zero volume-change conditions were applied by constantly adapting deformations of the assemblies in x and y directions such that $(1 + \varepsilon_{xx})(1 + \varepsilon_{yy})(1 + \varepsilon_{zz}) = 1$. Figures 3 and 4 show the undrained behavior for these two DEM assemblies in triaxial tests, respectively. The undrained stress paths of the two DEM assemblies shown in Fig. 3 depict the constitutive responses of Nevada sand observed in the laboratory tests, i.e., the stress-paths converge to substantially the same CSLs in both extension and compression tests at larger strains. During extension tests, strain softening behaviors are observed at small strains, followed by a pickup of strength at phase transformation (PT) points. It can be seen that a good match occurred in the TC tests at confining pressure $p' = 80$ kPa and $p' = 160$ kPa. However, the small strain portion in $p' = 40$ kPa compression tests differed from the experiment curve. Better overall agreement is achieved at assembly with $e_0 = 0.707$. The q -axial strain curves predicted by DEM simulations in Fig. 4 exhibit the correct trend with the experiment data in small strain regime.

Figures 5 and 6 show the DEM simulations along with the experimental results of drained monotonic compression constant-p' tests with initial relative density of about 40%. Reasonably well
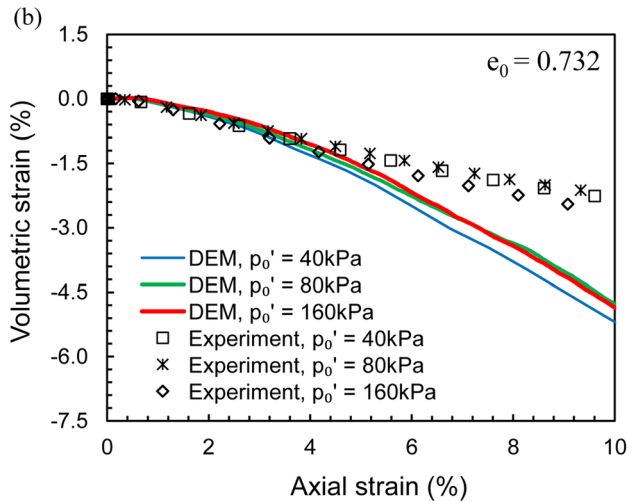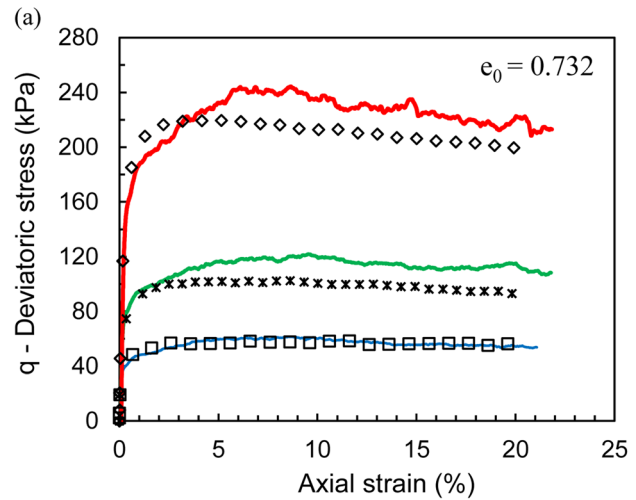
agreement in the $q - p'$ plots (Fig. 5(a)) with experimental results was achieved for both densities $e_0 = 0.732$ and $e_0 = 0.707$ at various confining pressures. The volumetric curves in Figs. 5(b) and 6(b) show that the calibrated DEM model can predict the volumetric strain reasonably well in the small strain region, particularly within 4%. Nevertheless, the discrepancy in volumetric responses gradually grows beyond this strain level, and the overprediction of volumetric strain in DEM becomes apparent, even though the deviatoric stress of the simulated and experimental simulations remains roughly compatible. This discrepancy in volumetric responses may be attributed to the discrepancy in particle shapes and arrangements, particle crashing, the oversimplification of contact laws, and the effect of boundary conditions. Presumably, incorporating microscopic experimental data via particle tracking techniques as well as more advanced DEM models to replicate the real particle shapes can reduce these discrepancies. These possible research directions will be explored in subsequent studies, but is out of the scope of this work.

The DEM predictions for 60% D_r triaxial tests under undrained and drained conditions are shown in Figs. 7–10. Two assemblies were considered for comparison with initial void ratios $e_0 = 0.674$ and $e_0 = 0.640$. Similar trends are observed in the 60% D_r drained and undrained tests.

The above figures showcase how well the high-fidelity DEM model replicates the pressure-sensitive responses of Nevada sand.
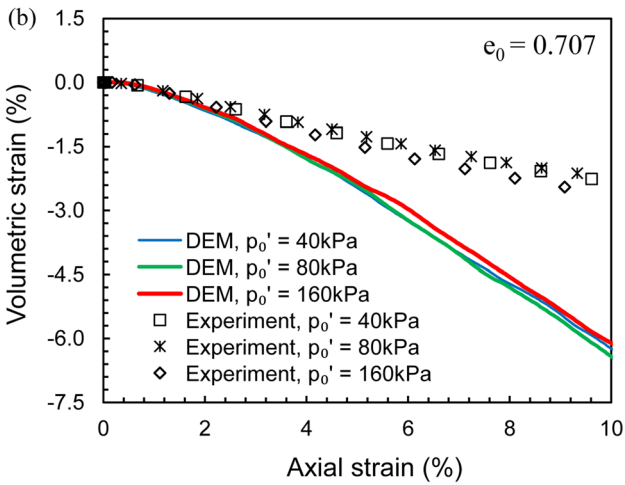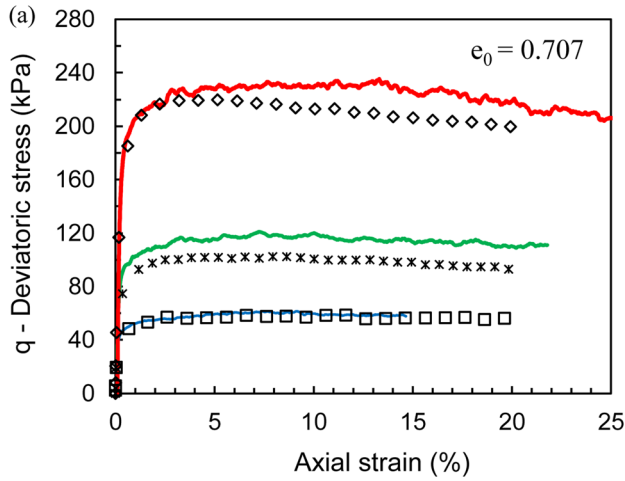
Fig. 6 Drained TC (constant p') of DEM simulations at $e = 0.707$, comparing with Nevada sand tests at relative density of 40% with initial confining pressure of 40 kPa, 80 kPa, and 160 kPa: (a) stress paths and (b) volumetric curves
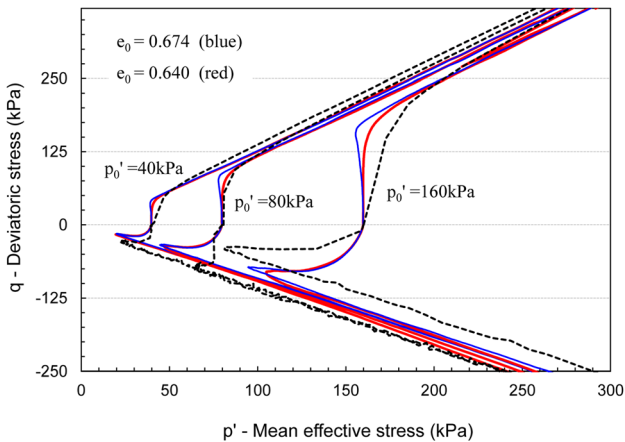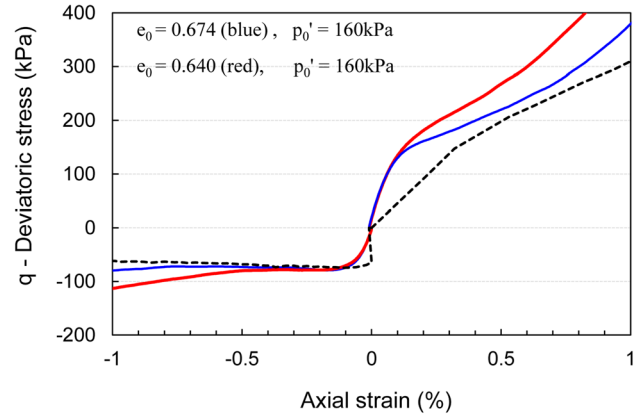

Fig. 7 Undrained TC and extension of DEM simulations at three densities, comparing with Nevada sand tests (black dashed lines) at relative density of 60% with initial confining pressure of 40 kPa, 80 kPa, and 160 kPa (stress paths)

We observe that the particle assemblies composed of bumpy particles are able to reproduce the shear responses and friction angles observed in triaxial experiments conducted at different confining pressure levels. Nevertheless, a sizable discrepancy in volumetric

Fig. 8 Undrained TC and extension of DEM simulations at three densities, comparing with Nevada sand tests (black dashed lines) at relative density of 60% with initial confining pressure of 160 kPa (stress–strain curves)
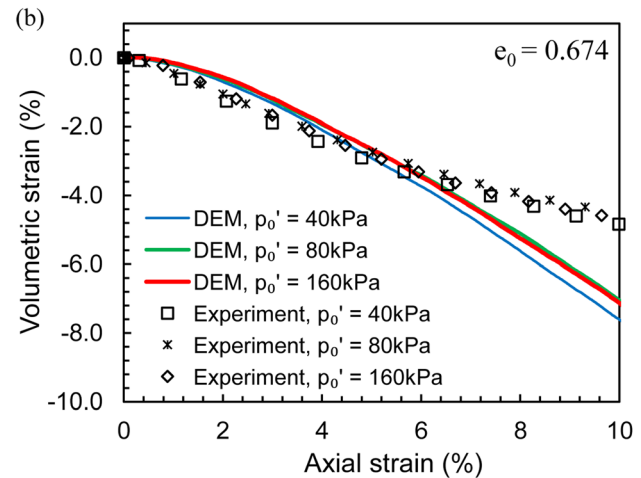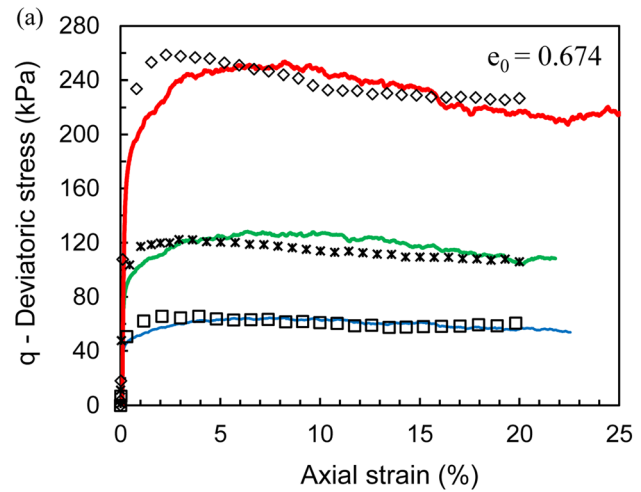

Fig. 9 Drained TC (constant p') of DEM simulation at $e_0 = 0.674$, comparing with Nevada sand tests at relative density of 60% with initial confining pressure of 40 kPa, 80 kPa, and 160 kPa: (a) stress paths and (b) volumetric curves

responses at finite deformation range is also noticed. These results imply that the DEM model currently employed in this study is a reasonably high-fidelity model when the strain-level is small. Nevertheless, caution must be exercised when interpreting the
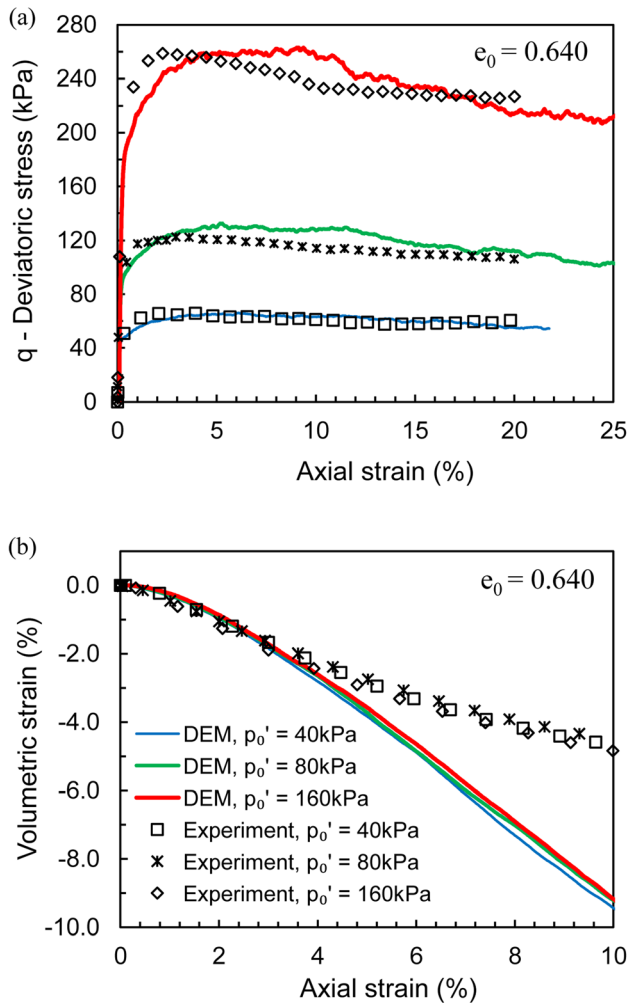
Fig. 10 Drained TC (constant p') of DEM simulations at $e_0 = 0.640$, comparing with Nevada sand tests at relative density of 60% with initial confining pressure of 40 kPa, 80 kPa, and 160 kPa: (*a*)stress paths and (*b*)volumetric curves

Fig. 11 Application of major, intermediate and minor principal stresses, σ_1, σ_2, and σ_3, to DEM assemblies in true triaxial tests to achieve all directions in the stress ratio π-plane (s_1, s_2, and s_3 denote the deviatoric principal stresses) [81]

volumetric responses from the extended database. It is also worthy to mention that results from Ref. [71] illustrated that the shear responses may be artificially stiffen if the load increment is too large. To avoid this issue, the same load increment $\Delta\varepsilon_{zz} = \pm 5.0 \times 10^{-7}$ was used for all of the DEM simulations in this paper.

3.3 Database Expansion With Virtual Tests. The experimental database was supplemented by simulated constitutive responses obtained from DEM simulations. These DEM simulations are conducted with particle assemblies of compatible relative densities and with grain-scale contact law parameters calibrated from experimental data. In the numerical examples, we limit our scopes on predicting the stress paths that were initially isotropic. Hence, the virtual database will only contain stress path of particle assemblies that were initially isotropically consolidated. The stress paths used for database expansion include (1) monotonic undrained TC, triaxial extension (TE), and simple shear (SS) tests; (2) monotonic drained conventional TC (CTC) tests; (3) monotonic true triaxial tests with constant mean effective stresses and various loading paths quantified by the intermediate principal stress ratio $b = (\sigma'_2 - \sigma'_3)/(\sigma'_1 - \sigma'_3)$ (as shown in Fig. 11) [81]; and (4) cyclic undrained unidirectional SS and TC tests. In this study, 15 DEM assemblies were considered with initial void ratios $e = 0.898, 0.789, 0.785, 0.783, 0.767, 0.746, 0.734, 0.707, 0.674, 0.640, 0.609, 0.577, 0.550, 0.529, 0.512$
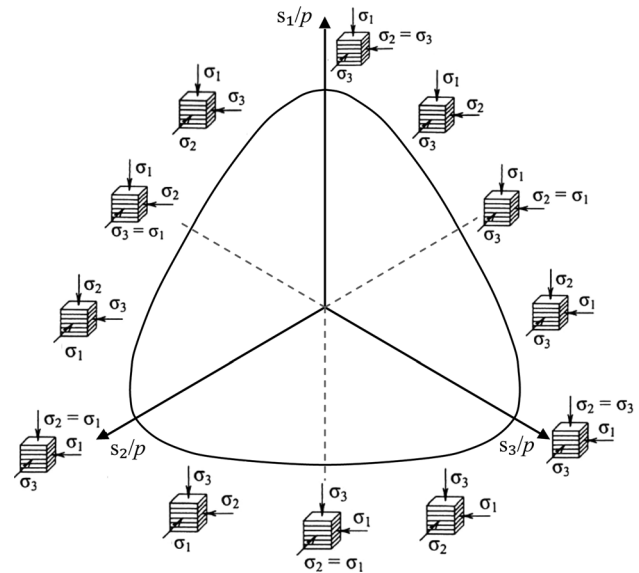
which were preconsolidated to different confining pressures $p_0 = 40, 80, 100, 160, 200, 300, 400 \, \text{kPa}$. These initial assemblies were then subjected to different loading paths to expand the experimental database. True triaxial stress paths are simulated via the servo-wall mechanism introduced in Ref. [82]. The major, intermediate, and minor principal stresses σ'_1, σ'_2, and σ'_3 are controlled by adjusting the tractions exerted on the walls such that the intermediate principal stress ratio b can be held consistently for the given stress path, as shown in Fig. 11.

4 Identification of Dafalias–Manzari Model Parameters

In this section, we present the procedure to identify material parameters using the EDD concept. We herein use one of the most commonly used critical state plasticity model, Dafalias–Manzari (DaMa) model [30], as an example to illustrate how EDD is built, calibrated, and utilized for material characterization. We want to emphasize that the proposed EDD procedure is applicable to other path-dependent materials.

4.1 Identification of DaMa Model Parameters. In order to predict the response of soils via a macroscopic constitutive model, it is necessary to determine the initial material state, drainage condition, and the model parameters. The initial state of soil is described by parameters include the initial effective confining pressure, p'_0, and initial void ratio, e_0. A set of 15 parameters is required to completely define the two-surface elastoplastic model in a fully three-dimensional space. These parameters can be grouped into three categories: (i) elastic parameters, G_0, ν; (ii) critical state parameters, $M, c, e^c_0, \lambda, \xi$; and (iii) model parameters such as state parameter constants n^b, n^d yield surface parameter m, hardening constants h_0, c_h, dilatancy parameter A_0, and fabric-dilatancy constants $z_{\max}, c_z$.

In a conventional calibration procedure for determining DaMa model parameters, a two-step calibration process is needed. In step 1, the elastic and critical state parameters are first manually determined with a high accuracy directly from experimental test data. The parameter of elastic shear modulus G_0 and Poisson's ratio ν is path independent and can be obtained from least square regression of the small strain monotonic shearing behavior at various confining pressures. We assume that the critical state

constants $M, c, e_0^c, \lambda, \xi$ for a given soil are independent of initial state and loading condition. Therefore, the critical state can be determined through curve fitting from a plot of triaxial test data that approach the critical state in $e - p/p_{\mathrm{at}}$ space. In step 2, the model specific parameters can be obtained by trial-and-error or through a numerical optimization procedure. In many situations, attention must be paid such that the material parameters used in the DaMa model would not lead to spurious numerical instability, especially when the mean effective stress is low [33]. In our implementation, we assume all the tests have the equal weights $w_i = 1$ for simplicity.

4.2 Parameter Identification for Nevada Sand. In this section, a comparison of DaMa model simulations and DEM trained data corresponding to monotonic triaxial tests is presented. DaMa model parameters have been calibrated based on existing laboratory experiments in Refs. [32] and [58] for Nevada sand. Andrade et al. [58] calibrated the DaMa model parameters to four undrained triaxial tests on Nevada sand performed by Yamamuro and Covert [83] for initial confining pressure $p_0' = 200 \, \mathrm{kPa}$ and $p_0' = 350 \, \mathrm{kPa}$ with void ratios $e_0 = 0.699$ and $e_0 = 0.711$. Shahir et al. [32] identified a set of parameter using nine experiments reported in Ref. [62] including seven monotonic drained and undrained TC tests and two undrained cyclic tests with relative density of about 40% and 60%. Though good agreements were achieved with experiments which were simulated in the aforementioned works, the simple loading conditions and limited number of the experimental tests may not provide enough constrains in the calibration process to capture the comprehensive material behavior. The large set of data in the EDD obtained from versatile virtual experiments solves this issue. The material parameters presented in Refs. [32] and [58] are used as initial guesses while calibrating the DaMa model in this study. To study the sensitivity of model parameters on different types of tests, material parameters are calibrated against tests under combinations of different initial material states, drainage conditions, and loading conditions for Nevada sand. The calibrated material parameters are listed in Table 3. Material constants presented by Andrade et al. [58] and Shahir et al. [32] are also given in Table 3 for comparison.

4.2.1 Critical State. The critical state surface is introduced in the DaMa model to incorporate the critical state soil mechanics concept into the bounding surface plasticity model. When the critical state is reached, both the bounding surface and dilatancy surface converge to the critical state surface in the stress space. On the other hand, both the hardening rule and the amount of plastic dilatation is dictated by the distance between both bounding surfaces to the critical state surface, and the dilatancy surface to the critical state surface, respectively. Therefore, determining the location of the critical state surface via calibrating the critical state parameters is crucial to the forward prediction capacity of the calibrated DaMa model. The DEM assemblies were deformed through the critical state so as to simulate the critical state responses of Nevada sand. The critical state parameters that locate the CSLs in the effective stress and state paths are identified. In the calibration process, a constrained optimization procedure is first run to determining the set of the critical state parameters $M, c, e_0^c, \lambda, \xi$ that minimize the errors measured by the objective function. Figure 12 plots the critical state surface in the stress ratio π-plane corresponding to the calibrated parameters set case *12b* in Table 3. The loading paths for drained true triaxial tests predicted by DEM simulations and the loading paths for the lab experiments are also shown in Fig. 12. As seen from Fig. 12, conventional lab experiments are conducted in limited loading paths, i.e., TC ($b = 0$) and TE ($b = 1$). While using DEM, under constant p' constraint, σ_1', σ_2', and σ_3' were controlled based on Fig. 11 to achieve constant b conditions, with b values representing different loading directions. The monotonic triaxial tests considered in the calibration help improve the DaMa model prediction of deviatoric plastic strain under radial monotonic loading.

4.2.2 Monotonic Triaxial Tests. Figures 13–16 show the constitutive responses simulated by the DaMa model in monotonic drained CTC tests for samples of various relative densities and initial confining pressures. The parameters referred as case *12b* in Table 3 were used in this set of simulations. The comparison between DEM trained data and DaMa model predicted results are presented in terms of q versus axial strain, and e versus p' plots. These results show the model can produce a reasonably well prediction of Nevada sand behavior for a broader range of densities and initial mean confining pressures using one set of parameters.

Figure 17 depicts DaMa model prediction results of $q - p'$ responses (case *12a* in Table 3) for monotonic undrained TC tests. The overall trend of the sand behavior under undrained compression is well captured. It can be observed that in higher density and lower confining pressure samples, the sand is highly dilatant, while in lower density and higher confining pressure samples, the opposite effect is observed. Good agreement of the $q - p'$ responses is obtained for loose and medium dense samples (i.e., $e_0 = 0.783$ and 0.720). However, the DaMa model predicts larger

Table 3   Model parameters of the DaMa model calibrated for Nevada sand

Parameter function	Parameter index	Andrade et al. [58]	Shahir et al. [32]	Case *12a*	Case *1b*	Case *2b*	Case *12b*	Case *2a*#*
Elasticity	G_0	125	150	150	150	150	150	150
	v	0.05	0.05	0.05	0.05	0.05	0.05	0.05
Critical state	M	1.45	1.14	1.14	1.34	1.34	1.34	1.08
	c	0.78	0.78	0.78	0.78	0.78	0.78	0.78
	λ_c	0.09	0.027	0.098	1.13	1.13	1.13	0.09
	e_0^c	0.737	0.83	0.833	0.833	0.833	0.912	0.73
	ξ	1.0	0.45	0.12	0.12	0.12	0.12	1.0
Yield surface	m	0.01	0.02	0.02	0.02	0.02	0.02	0.02
Plastic modulus	h_0	4.5	9.7	9.7	9.416	9.416	9.402	9.25
	c_h	1.05	1.02	1.02	1.2	1.28	1.21	1.03
	n^b	1.1	2.56	2.56	2.038	2.038	1.307	1.49
Dilatancy	A_0	0.804	0.81	0.81	0.81	0.796	0.85	0.81
	n^d	5.5	1.05	1.05	5.78	1.014	1.78	4.98
Fabric-dilatancy	$z_{\max}$	10	5	5	5	5	5	10
	c_z	500	800	800	800	800	800	500

Note: Italic symbols appeared after cases have the meaning as follows: *1* denotes loose–medium dense samples, *2* denotes medium dense–dense sample, *a* denotes monotonic undrained triaxial tests, *b* denotes monotonic drained triaxial tests, * denotes tests with variable loading paths, and # denotes loading–unloading tests.
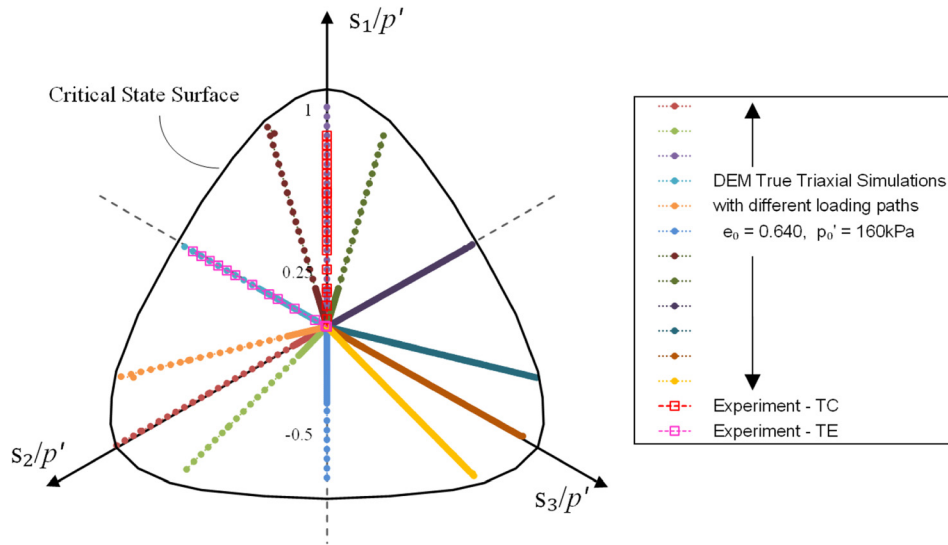
Fig. 12 Calibrated critical state surface for DaMa model, and the loading paths of monotonic triaxial tests for DEM simulations and lab experiments [62] in the stress ratio π-plane (s_1, s_2, and s_3 denote the deviatoric principal stresses)
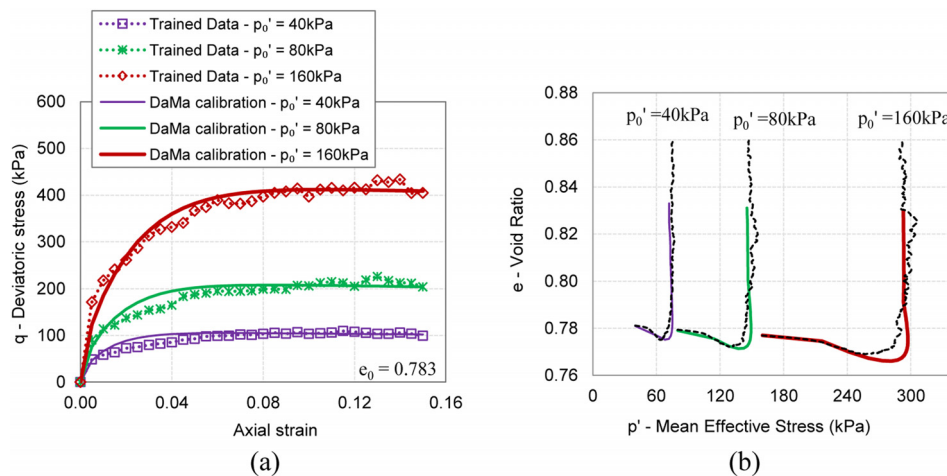

Fig. 13 DaMa model calibration for CTC tests on samples with different initial confining pressures ($e_0 = 0.783$). (*a*) *q* versus axial strain and (*b*) void ratio versus mean effective stress.

slopes of the CSL at large strains for dense samples than what is expected in the trained data.

5   Assessment of Forward Predictions With Calibrated Dafalias–Manzari Model

In this study, a subset of the data in the EDD, which is called the verification/test set, is purposely excluded from being used for material identifications of both the high- and low-fidelity models (see Fig. 1). Instead, these unused data are employed to assess the accuracy and robustness of forward predictions. The verification set consists of experiments from both the laboratory tests and the virtual simulations. In this assessment study, we conduct the predicted simulations using the calibrated DaMa model and compare the predicted results with this subset of experimental data that have purposely not used for calibration. Figure 18 shows comparisons between predictions from DaMa model and verification data for monotonic TC tests. The verification tests consist of both drained and undrained TC loading paths of an isotropically consolidated Nevada sand, in which the DEM virtual simulations are conducted with densities $e_0 = 0.707$ and 0.529 under initial mean effective pressure $p_0' = 100$, 200, and 300 kPa, respectively. The

experimental data from Ref. [84] for Nevada sand with $D_r = 65\%$ and initial mean effective pressure $p_0' = 100$, 250, and 400 kPa are also compared with DaMa model prediction (see Fig. 18(*c*)). The stress–strain relation shown in Fig. 18 indicates that the calibrated DaMa model can produce a reasonably good prediction of Nevada sand behavior for the tests in the verification set of EDD. Comparisons of results from Figs. 18(*a*) and 18(*b*) suggest that the calibrated DaMa model replicates the strain–strain curves more accurately at the drained limit than those at the undrained limit. Nevertheless, both the drained and undrained simulation results are able to predict the friction angle at steady-state well. These well-matched responses are encouraging given the fact that there is no microstructural information available to calibrate the high-fidelity DEM model and there is no attempt to explicitly model the particle shape variation in this study.

Another assessment test we conducted is a comparison between the simulated undrained cyclic SS loading responses predicted by the calibrated DaMa model and the experimental data reported in Ref. [62] for Nevada sand with $D_r = 40\%$ and $p_0' = 80$ kPa. The purpose of this test is to assess how well the calibrated low-fidelity model predict loading paths not included in the EDD database. Such a test is important, as the loading history of soils is
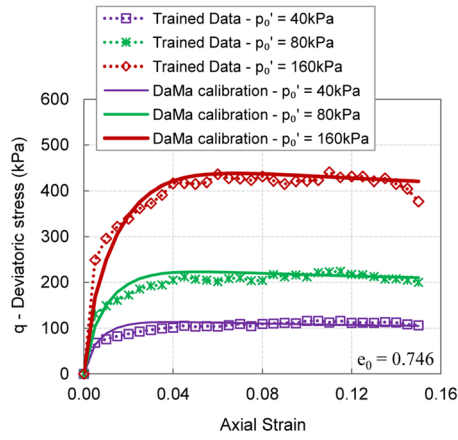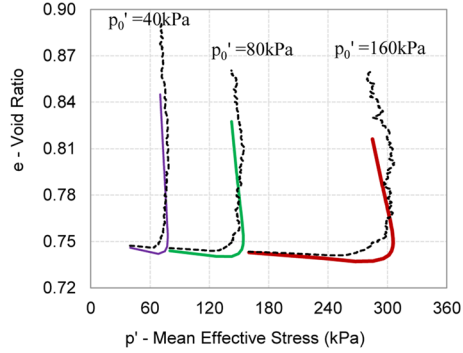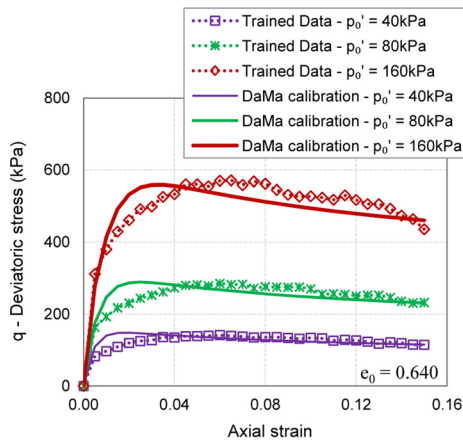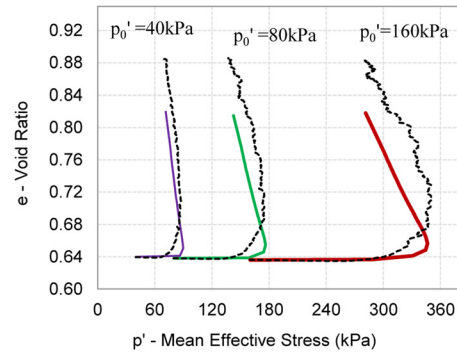
Fig. 14 DaMa model calibration for CTC tests on samples with different initial confining pressures ($e_0 = 0.746$). (*a*) *q* versus axial strain and (*b*) void ratio versus mean effective stress.
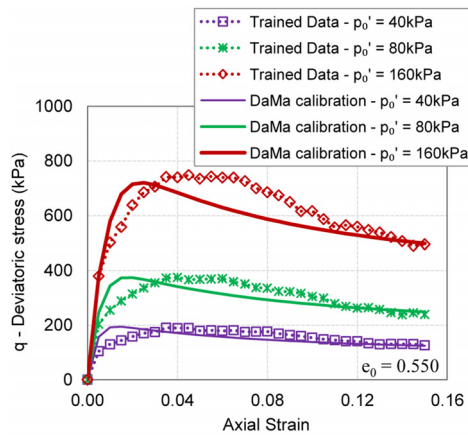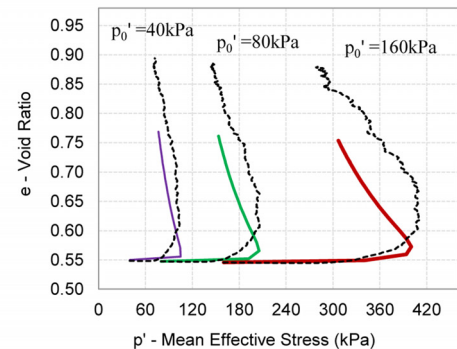

Fig. 15 DaMa model calibration for CTC tests on samples with different initial confining pressures ($e_0 = 0.640$). (*a*) *q* versus axial strain and (*b*) void ratio versus mean effective stress.

Fig. 16 DaMa model calibration for CTC tests on samples with different initial confining pressures ($e_0 = 0.550$). (*a*) *q* versus axial strain and (*b*) void ratio versus mean effective stress.
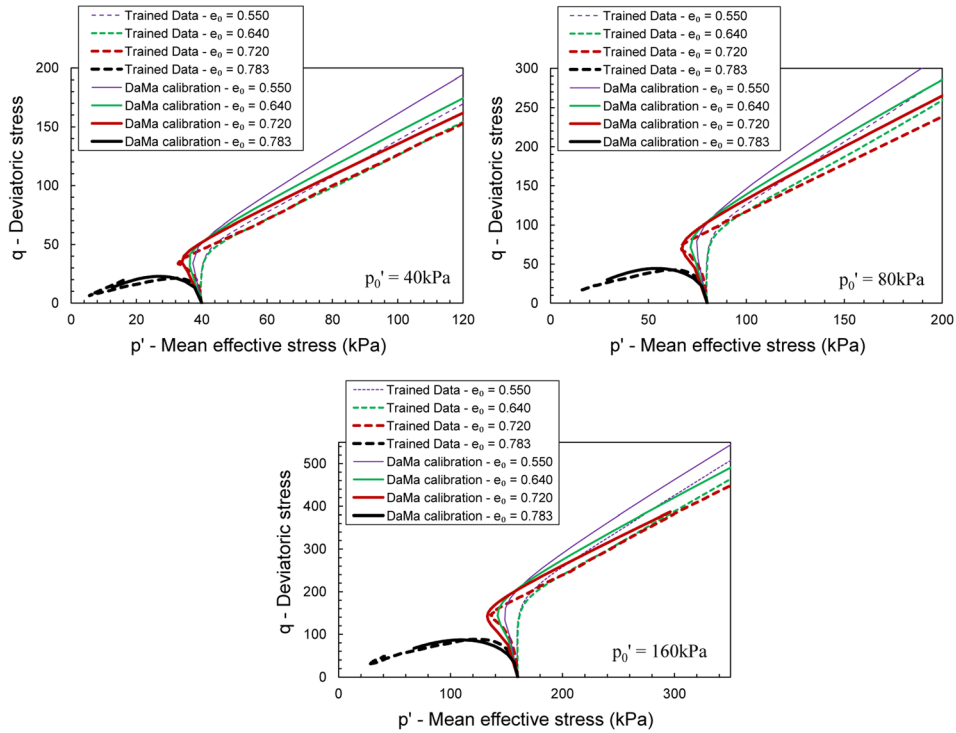
Fig. 17 DaMa model calibration of $q-p\prime$ responses for monotonic undrained TC tests on samples with different initial confining pressures and densities
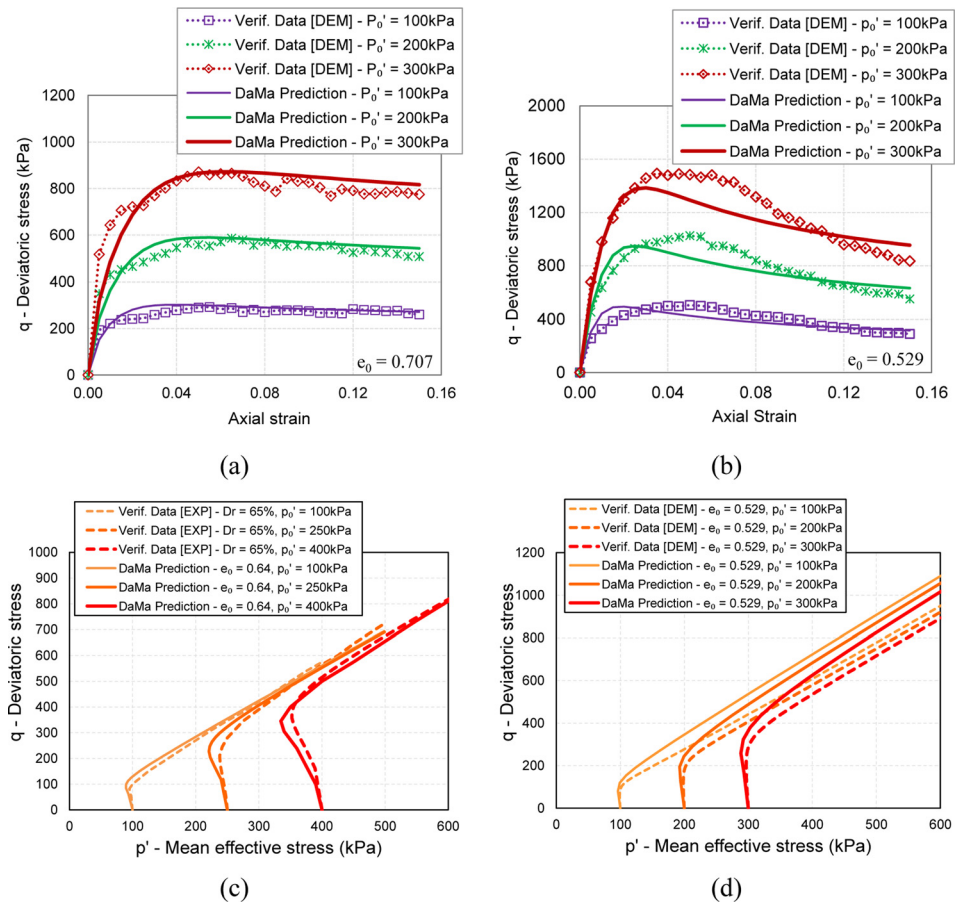

Fig. 18 Comparison between verification data and DaMa model prediction for: (*a*) and (*b*) drained monotonic CTC tests, and (*c*) and (*d*) undrained TC tests (experimental data in (*c*) are from Ref. [82])
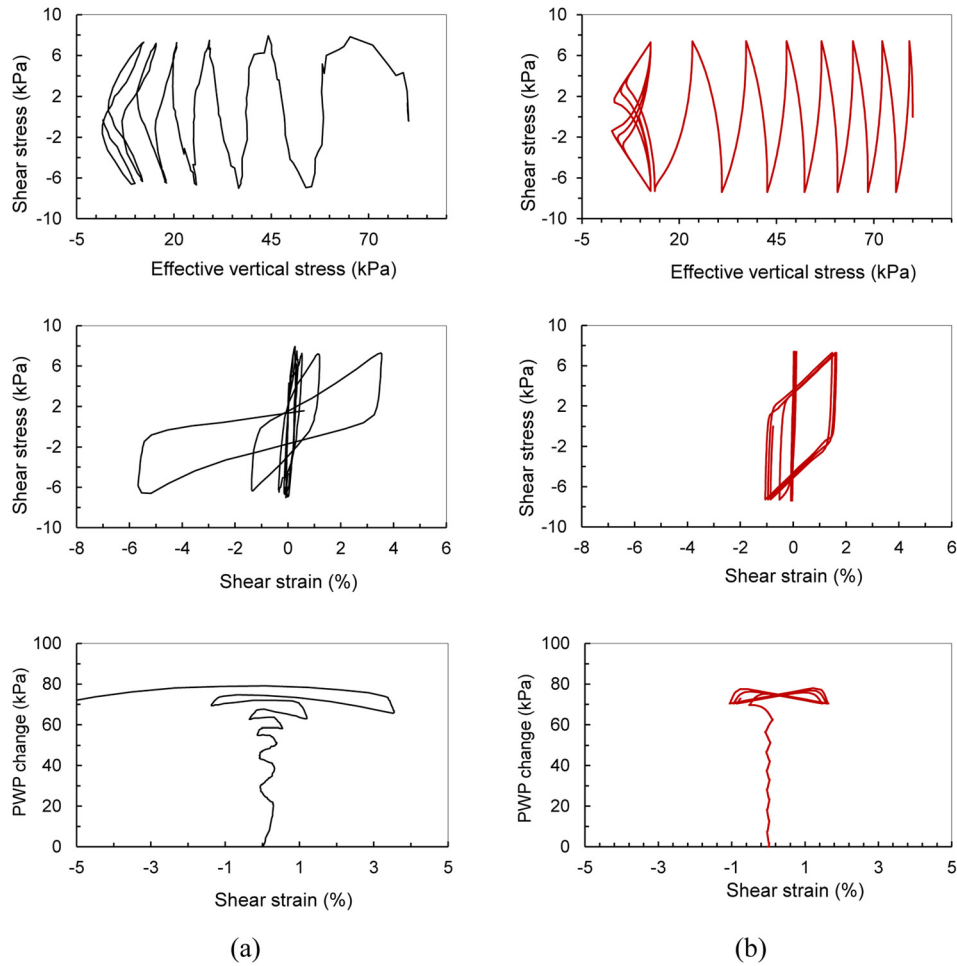
Fig. 19 Undrained cyclic SS test for Nevada sand: Dr = 40% and p'_0 = 80 kPa: (a) experimental data from Ref. [62]; (b) Dafalias–Manzari model predictions

often significantly different and more complicated than the idealized cases studied in the laboratory. The cyclic test was numerically simulated using the DaMa model with parameters of case *2a*# as reported in Table 3. In this test, cyclic shearing was applied in the horizontal direction in a load-controlled manner with a cyclic stress amplitude of ±7.4 kPa. Figure 19 compares curves of the shear stress versus mean effective stress, shear stress versus shear strain, and PWP change versus shear train, obtained from both lab experiment and DaMa model prediction. The comparison shows that the DaMa model predictions are qualitatively consistent with the experimental responses. Similar to what was observed in the monotonic tests, the discrepancy become evident in the large strain region as shown in the shear stress versus shear strain curve. The inaccurate prediction for the cyclic test by DaMa model may be attributed to the fact that most of the experiments used to construct the database are monotonic and the DEM model does not reflect the real geometrical features of grains; therefore, the parameters calibrated based on such database cannot accurately capture the cyclic responses in which the material may undergo very complex behaviors, such as multiple PT. In addition, the DaMa model used in this study is a small strain plasticity model and does not incorporate the geometrical nonlinearity. We found that the accuracy and robustness of the low-fidelity surrogate model reduce when the simulated loading paths are different from those available from the experimental data (e.g., drained versus undrained, monotonic versus cyclic). This observation is consistent of the previous studies [18,33]. Presumably, those issues can be resolved by incorporating more advanced high-fidelity method, such as granular element method [85] to extend the

material database more accurately, and/or more comprehensive constitutive models that incorporate more detailed mechanisms, such as fabric changes, cyclic mobility, and geometrical nonlinearity. Those studies will be considered in the future study but is out of the scope of this work.

6 Conclusions

In this paper, we present a new simulation-based database extension technique aimed at calibrating comprehensive critical state plasticity models with limited available experimental data. By utilizing a high-fidelity model (DEM) that has been calibrated against experiments, additional high-fidelity simulations are used to supplement experimental data by the so-called EDD. The EDD essentially provide additional constraints for identifying the optimized parameter set for the low-fidelity phenomenological constitutive models. When experimental data is expensive to generate or inaccessible, this approach provides a much-needed alternative. Numerical experiments conducted herein show that the proposed multilevel calibration approach is capable of obtaining material parameters for capturing the behavior of cohesion-less sand under various drainage and monotonic loading conditions, void ratios, and confining pressures at the small deformation range, but the results are less satisfactory for cyclic and large deformation problems.

References

[1] DiMaggio, F. L., and Sandler, I. S., 1971, "Material Model for Granular Soils," J. Eng. Mech. Div., **97**(3), pp. 935–950.

[2] Finn, W. L., Lee, K. W., and Martin, G., 1977, "An Effective Stress Model for Liquefaction," Electron. Lett., **103**, pp. 517–533.

[3] Prevost, J. H., 1985, "A Simple Plasticity Theory for Frictional Cohesionless Soils," Int. J. Soil Dyn. Earthquake Eng., **4**(1), pp. 9–17.

[4] Bardet, J., 1986, "Bounding Surface Plasticity Model for Sands," J. Eng. Mech., **112**(11), pp. 1198–1217.

[5] Anandarajah, A., 1993, "VELACS Project: Elasto-Plastic Finite Element Prediction of the Liquefaction Behavior of Centrifuge Models Nos. 1, 3 and 4a," International Conference on the Verification of Numerical Procedures for the Analysis of Soil Liquefaction Problems, Balkema, Rotterdam, The Netherlands.

[6] Oka, F., Adachi, T., and Yashima, A., 1995, "A Strain Localization Analysis Using a Viscoplastic Softening Model for Clay," Int. J. Plast., **11**(5), pp. 523–545.

[7] Borja, R. I., Chao, H., Montáns, F., and Lin, C., 1999, "Nonlinear Ground Response at Lotung LSST Site," J. Geotech. Geoenviron. Eng., **125**(3), pp. 187–197.

[8] Jeremic, B., Runesson, K., and Sture, S., 1999, "A Model for Elastic-Plastic Pressure Sensitive Materials Subjected to Large Deformations," Int. J. Solids Struct., **36**(31), pp. 4901–4918.

[9] Nemat-Nasser, S., and Zhang, J., 2002, "Constitutive Relations for Cohesionless Frictional Granular Materials," Int. J. Plast., **18**(4), pp. 531–547.

[10] Lashkari, A., and Latifi, M., 2008, "A Non-Coaxial Constitutive Model for Sand Deformation Under Rotation of Principal Stress Axes," Int. J. Numer. Anal. Methods Geomech., **32**(9), pp. 1051–1086.

[11] Yang, Z., and Elgamal, A., 2008, "Multi-Surface Cyclic Plasticity Sand Model With Lode Angle Effect," Geotech. Geol. Eng., **26**(3), pp. 335–348.

[12] Andrade, J. E., and Ellison, K. C., 2008, "Evaluation of a Predictive Constitutive Model for Sands," J. Geotech. Geoenviron. Eng., **134**(12), pp. 1825–1828.

[13] Li, L., Aubertin, M., and Shirazi, A., 2010, "Implementation and Application of a New Elastoplastic Model Based on a Multiaxial Criterion to Assess the Stress State Near Underground Openings," Int. J. Geomech., **10**(1), pp. 13–21.

[14] Roscoe, K. H., Schofield, A., and Wroth, C., 1958, "On the Yielding of Soils," Geotechnique, **18**(1), pp. 22–53.

[15] Schofield, A., and Wroth, P., 1968, Critical State Soil Mechanics, McGraw-Hill, London.

[16] Roscoe, K. H., and Burland, J., 1968, On The Generalized Stress-Strain Behaviour of Wet Clay, Cambridge University Press, London.

[17] Nova, R., and Wood, D. M., 1979, "A Constitutive Model for Sand in Triaxial Compression," Int. J. Numer. Anal. Methods Geomech., **3**(3), pp. 255–278.

[18] Manzari, M. T., and Dafalias, Y. F., 1997, "A Critical State Two-Surface Plasticity Model for Sands," Geotechnique, **47**(2), pp. 255–272.

[19] Jefferies, M., 1993, "Nor-Sand: A Simple Critical State Model for Sand," Géotechnique, **43**(1), pp. 91–103.

[20] Borja, R. I., and Lee, S. R., 1990, "Cam-Clay Plasticity, Part 1: Implicit Integration of Elasto-Plastic Constitutive Relations," Comput. Methods Appl. Mech. Eng., **78**(1), pp. 49–72.

[21] Borja, R. I., and Andrade, J. E., 2006, "Critical State Plasticity. Part VI: Meso-Scale Finite Element Simulation of Strain Localization in Discrete Granular Materials," Comput. Methods Appl. Mech. Eng., **195**(37), pp. 5115–5140.

[22] Gao, Z., Zhao, J., Li, X.-S., and Dafalias, Y. F., 2014, "A Critical State Sand Plasticity Model Accounting for Fabric Evolution," Int. J. Numer. Anal. Methods Geomech., **38**(4), pp. 370–390.

[23] Tanaka, M., and Dulikravich, G. S., 1998, Inverse Problems in Engineering Mechanics, Elsevier, Amsterdam.

[24] Chaparro, B. M., Thuillier, S., Menezes, L. F., Manach, P. Y., and Fernandes, J. V., 2008, "Material Parameters Identification: Gradient-Based, Genetic and Hybrid Optimization Algorithms," Comput. Mater. Sci., **44**(2), pp. 339–346.

[25] Yang, Z., and Elgamal, A., 2003, "Application of Unconstrained Optimization and Sensitivity Analysis to Calibration of a Soil Constitutive Model," Int. J. Numer. Anal. Methods Geomech., **27**(15), pp. 1277–1297.

[26] Blaheta, R., Hrtus, R., Kohut, R., Axelsson, O., and Jakl, O., 2012, "Material Parameter Identification With Parallel Processing and Geo-Applications," Parallel Processing and Applied Mathematics, Springer, Berlin, Heidelberg, pp. 366–375.

[27] Feng, X.-T., Chen, B.-R., Yang, C., Zhou, H., and Ding, X., 2006, "Identification of Visco-Elastic Models for Rocks Using Genetic Programming Coupled With the Modified Particle Swarm Optimization Algorithm," Int. J. Rock Mech. Min. Sci., **43**(5), pp. 789–801.

[28] Ghaboussi, J., Pecknold, D. A., Zhang, M., and Haj-Ali, R. M., 1998, "Autoprogressive Training of Neural Network Constitutive Models," Int. J. Numer. Methods Eng., **42**(1), pp. 105–126.

[29] Li, X., 2005, "Calibration of an Anisotropic Sand Model," Calibration of Constitutive Models, ASCE, pp. 1–12.

[30] Dafalias, Y. F., and Manzari, M. T., 2004, "Simple Plasticity Sand Model Accounting for Fabric Change Effects," J. Eng. Mech., **130**(6), pp. 622–634.

[31] Papadimitriou, A. G., and Bouckovalas, G. D., 2002, "Plasticity Model for Sand Under Small and Large Cyclic Strains: A Multiaxial Formulation," Soil Dyn. Earthquake Eng., **22**(3), pp. 191–204.

[32] Shahir, H., Pak, A., Taiebat, M., and Jeremic, B., 2012, "Evaluation of Variation of Permeability in Liquefiable Soil Under Earthquake Loading," Comput. Geotech., **40**, pp. 74–88.

[33] Choi, C., Arduino, P., and Harney, M. D., 2005, "Two-Surface Soil Constitutive Model Calibration for Coarse Granular Materials," Calibration of Constitutive Models, ASCE, pp. 1–15.

[34] Mahnken, R., and Stein, E., 1994, "The Identification of Parameters for Visco-Plastic Models Via Finite-Element Methods and Gradient Methods," Modell. Simul. Mater. Sci. Eng., **2**(3A), pp. 597–616.

[35] Mahnken, R., and Stein, E., 1996, "A Unified Approach for Parameter Identification of Inelastic Material Models in the Frame of the Finite Element Method," Comput. Methods Appl. Mech. Eng., **136**(3), pp. 225–258.

[36] Rechenmacher, A. L., and Medina-Cetina, Z., 2007, "Calibration of Soil Constitutive Models With Spatially Varying Parameters," J. Geotech. Geoenviron. Eng., **133**(12), pp. 1567–1576.

[37] Arnold, S. M., Holland, F., and Bednarcyk, B. A., 2014, "Robust Informatics Infrastructure Required for ICME: Combining Virtual and Experimental Data," 55th AIAA/ASMe/ASCE/AHS/SC Structures, Structural Dynamics, and Materials Conference.

[38] Broderick, S. R., Aourag, H., and Rajan, K., 2011, "Data Mining of Ti–Al Semi-Empirical Parameters for Developing Reduced Order Models," Phys. B, **406**(11), pp. 2055–2060.

[39] Feng, X. T., and Yang, C., 2004, "Coupling Recognition of the Structure and Parameters of Non-Linear Constitutive Material Models Using Hybrid Evolutionary Algorithms," Int. J. Numer. Methods Eng., **59**(9), pp. 1227–1250.

[40] Alexandrov, N. M., Lewis, R. M., Gumbert, C. R., Green, L. L., and Newman, P. A., 1999, "Optimization With Variable-Fidelity Models Applied to Wing Design," AIAA Paper No. 2000-0841.

[41] Alexandrov, N. M., Dennis, J. E., Jr., Lewis, R. M., and Torczon, V., 1998, "A Trust-Region Framework for Managing the Use of Approximation Models in Optimization," Struct. Optim., **15**(1), pp. 16–23.

[42] Cundall, P. A., and Strack, O. D., 1979, "A Discrete Numerical Model for Granular Assemblies," Geotechnique, **29**(1), pp. 47–65.

[43] Sun, W., Kuhn, M. R., and Rudnicki, J. W., 2013, "A Multiscale DEM-LBM Analysis on Permeability Evolutions Inside a Dilatant Shear Band," Acta Geotech., **8**(5), pp. 465–480.

[44] Jäger, J., 1999, "Uniaxial Deformation of a Random Packing of Particles," Arch. Appl. Mech., **69**(3), pp. 181–203.

[45] Jaeger, J., 2005, New Solutions in Contact Mechanics, WIT Press/Computational Mechanics, Southampton, MA.

[46] Kuhn, M. R., 2011, "Implementation of the Jäger Contact Model for Discrete Element Simulations," Int. J. Numer. Methods Eng., **88**(1), pp. 66–82.

[47] Liu, Y., Sun, W., Yuan, Z., and Fish, J., 2015, "A Nonlocal Multiscale Discrete-Continuum Model for Predicting Mechanical Behavior of Granular Materials," Int. J. Numer. Methods Eng. (submitted).

[48] Christoffersen, J., Mehrabadi, M., and Nemat-Nasser, S., 1981, "A Micromechanical Description of Granular Material Behavior," ASME J. Appl. Mech., **48**(2), pp. 339–344.

[49] Satake, M., 1978, "Constitution of Mechanics of Granular Materials Through the Graph Theory," Continuum Mechanical and Statistical Approaches in the Mechanics of Granular Materials, Gakuzutsu Bunken Fukyukai, Tokyo, pp. 47–62.

[50] Pastor, M., Zienkiewicz, O., and Chan, A., 1990, "Generalized Plasticity and the Modelling of Soil Behaviour," Int. J. Numer. Anal. Methods Geomech., **14**(3), pp. 151–190.

[51] Pestana, J. M., and Whittle, A., 1995, "Compression Model for Cohesionless Soils," Géotechnique, **45**(4), pp. 611–631.

[52] Ling, H. I., and Yang, S., 2006, "Unified Sand Model Based on the Critical State and Generalized Plasticity," J. Eng. Mech., **132**(12), pp. 1380–1391.

[53] Jefferies, M., and Been, K., 2000, "Implications for Critical State Theory From Isotropic Compression of Sand," Géotechnique, **50**(4), pp. 419–429.

[54] Wood, D. M., 1990, Soil Behaviour and Critical State Soil Mechanics, Cambridge University, New York.

[55] Li, X.-S., and Wang, Y., 1998, "Linear Representation of Steady-State Line for Sand," J. Geotech. Geoenviron. Eng., **124**(12), pp. 1215–1217.

[56] Been, K., and Jefferies, M. G., 1985, "A State Parameter for Sands," Géotechnique, **35**(2), pp. 99–112.

[57] Nazzal, M. D., Abu-Farsakh, M. Y., and Mohammad, L. N., 2010, "Implementation of a Critical State Two-Surface Model to Evaluate the Response of Geosynthetic Reinforced Pavements," Int. J. Geomech., **10**(5), pp. 202–212.

[58] Andrade, J. E., Ramos, A. M., and Lizcano, A., 2013, "Criterion for Flow Liquefaction Instability," Acta Geotech., **8**(5), pp. 525–535.

[59] Conn, A. R., Gould, N. I., and Toint, P. L., 2000, Trust Region Methods, MPS/SIAM Series on Optimization, SIAM, Philadelphia, PA.

[60] Marquardt, D. W., 1963, "An Algorithm for Least-Squares Estimation of Nonlinear Parameters," J. Soc. Ind. Appl. Math., **11**(2), pp. 431–441.

[61] Fish, J., 2013, Practical Multiscaling, Wiley, New York.

[62] Arulmoli, K., 1992, Velacs Verification of Liquefaction Analyses by Centrifuge Studies Laboratory Testing Program: Soil Data Report, Earth Technology Corporation, Irvine, CA.

[63] Kammerer, A. M., Wu, J., Pestana, J. M., Riemer, M., and Seed, R. B., 2000, "Cyclic Simple Shear Testing of Nevada Sand for PEER Center Project

2051999," Dept. of Civil and Environmental Engineering, Univ. of California, Berkley, CA, Geotechnical Engineering Rep. No. UCB/GT/00- 01.

[64] Kuhn, M. R., 2008, "OVAL and OVALPLOT: Programs for Analyzing Dense Particle Assemblies With the Discrete Element Method," http://faculty.up.edu/kuhn/oval/oval.html

[65] Viggiani, G., Andò, E., Takano, D., and Santamarina, J. C., 2015, "Laboratory X-Ray Tomography: A Valuable Experimental Tool for Revealing Processes in Soils," Geotech. Test. J., 38(1), pp. 61–71.

[66] Charalampidou, E.-M., Hall, S. A., Stanchits, S., Lewis, H., and Viggiaini, G., 2011, "Characterization of Shear and Compaction Bands in a Porous Sandstone Deformed Under Triaxial Compression," Tectonophysics, 503(1), pp. 8–17.

[67] Sun, W., Andrade, J. E., Rudnicki, J. W., and Eichhubl, P., 2011, "Connecting Microstructural Attributes and Permeability From 3D Tomographic Images of In Situ Shear-Enhanced Compaction Bands Using Multiscale Computations," Geophys. Res. Lett., 38(10), p. L10302.

[68] Sun, W., Andrade, J. E., and Rudnicki, J. W., 2011, "Multiscale Method for Characterization of Porous Microstructures and Their Impact on Macroscopic Effective Permeability," Int. J. Numer. Methods Eng., 88(12), pp. 1260–1279.

[69] Boon, C., Houlsby, G., and Utili, S., 2012, "A New Algorithm for Contact Detection Between Convex Polygonal and Polyhedral Particles in the Discrete Element Method," Comput. Geotech., 44, pp. 73–82.

[70] Lim, K. W., and Andrade, J. E., 2014, "Granular Element Method for Three-Dimensional Discrete Element Calculations," Int. J. Numer. Anal. Methods Geomech., 38(2), pp. 167–188.

[71] Kuhn, M. R., Renken, H., Mixsell, A., and Kramer, S., 2014, "Investigation of Cyclic Liquefaction With Discrete Element Simulations," J. Geotech. Geoenviron. Eng., 140(12), p. 04014075.

[72] Salot, C., Gotteland, P., and Villard, P., 2009, "Influence of Relative Density on Granular Materials Behavior: DEM Simulations of Triaxial Tests," Granular Matter, 11(4), pp. 221–236.

[73] Hardin, B. O., 1985, "Crushing of Soil Particles," J. Geotech. Eng., 111(10), pp. 1177–1192.

[74] Cheng, Y., Bolton, M., and Nakata, Y., 2004, "Crushing and Plastic Deformation of Soils Simulated Using DEM," Geotechnique, 54(2), pp. 131–141.

[75] Lade, P. V., Yamamuro, J. A., and Bopp, P. A., 1996, "Significance of Particle Crushing in Granular Materials," J. Geotech. Eng., 122(4), pp. 309–316.

[76] ASTMD4253, 2006, "Standard Test Methods for Maximum Index Density and Unit Weight of Soils Using a Vibratory Table," ASTM International, West Conshohocken, PA.

[77] ASTMD4254, 2006, "Standard Test Methods for Minimum Index Density and Unit Weight of Soils and Calculation of Relative Density," ASTM International, West Conshohocken, PA.

[78] Hardin, B. O., 1978, "The Nature of Stress-Strain Behavior for Soils," Earthquake Engineering and Soil Dynamics—ASCE Geotechnical Engineering Division Specialty Conference, Pasadena, CA, Jun. 19–21.

[79] Wichtmann, T., and Triantafyllidis, T., 2009, "Influence of the Grain-Size Distribution Curve of Quartz Sand on the Small Strain Shear Modulus G_{max}," J. Geotech. Geoenviron. Eng., 135(10), pp. 1404–1418.

[80] Cho, G.-C., Dodds, J., and Santamarina, J. C., 2006, "Particle Shape Effects on Packing Density, Stiffness, and Strength: Natural and Crushed Sands," J. Geotech. Geoenviron. Eng., 132(5), pp. 591–602.

[81] Lade, P. V., 2008, "Failure Criterion for Cross-Anisotropic Soils," J. Geotech. Geoenviron. Eng., 134(1), pp. 117–124.

[82] Barreto, D., and O'Sullivan, C., 2012, "The Influence of Inter-Particle Friction and the Intermediate Stress Ratio on Soil Response Under Generalised Stress Conditions," Granular Matter, 14(4), pp. 505–521.

[83] Yamamuro, J. A., and Covert, K. M., 2001, "Monotonic and Cyclic Liquefaction of Very Loose Sands With High Silt Content," J. Geotech. Geoenviron. Eng., 127(4), pp. 314–324.

[84] Kutter, B. L., Chen, Y.-R., and Shen, C., 1994, "Triaxial and Torsional Shear Test Results for Sand," Naval Facilities Engineering Service Center. Port Hueneme, CA, Contract Report CR 94.003-SHR.

[85] Andrade, J. E., Lim, K.-W., Avila, C. F., and Vlahinic, I., 2012, "Granular Element Method for Computational Particle Mechanics," Comput. Methods Appl. Mech. Eng., 241–244, pp. 262–274.